



## How Does Plant Cell Wall Nanoscale Architecture Correlate with Enzymatic Digestibility?

Shi-You Ding *et al.*

*Science* **338**, 1055 (2012);

DOI: 10.1126/science.1227491

*This copy is for your personal, non-commercial use only.*

If you wish to distribute this article to others, you can order high-quality copies for your colleagues, clients, or customers by [clicking here](#).

Permission to republish or repurpose articles or portions of articles can be obtained by following the guidelines [here](#).

**The following resources related to this article are available online at [www.sciencemag.org](http://www.sciencemag.org) (this information is current as of November 22, 2012):**

**Updated information and services**, including high-resolution figures, can be found in the online version of this article at:

<http://www.sciencemag.org/content/338/6110/1055.full.html>

**Supporting Online Material** can be found at:

<http://www.sciencemag.org/content/suppl/2012/11/20/338.6110.1055.DC1.html>

This article **cites 40 articles**, 14 of which can be accessed free:

<http://www.sciencemag.org/content/338/6110/1055.full.html#ref-list-1>

This article appears in the following **subject collections**:

Chemistry

<http://www.sciencemag.org/cgi/collection/chemistry>

15. Materials and methods are available as supplementary materials on *Science* Online.
16. W. Benz, A. G. W. Cameron, H. J. Melosh, *Icarus* **81**, 113 (1989).
17. S. L. Thompson, H. S. Lauson, *Technical Rep. SC-RR-710714*, Sandia Nat. Labs (1972).
18. H. J. Melosh, *Meteorit. Planet. Sci.* **42**, 2079 (2007).
19. S. Ida, R. M. Canup, G. R. Stewart, *Nature* **389**, 353 (1997).
20. E. Kokubo, J. Makino, S. Ida, *Icarus* **148**, 419 (2000).
21. M. M. Meier, A. Reufer, W. Benz, R. Wieler, *Annual Meeting of the Meteoritical Society LXXIV*, abstr. 5039 (2011).
22. C. B. Agnor, R. M. Canup, H. F. Levison, *Icarus* **142**, 219 (1999).
23. D. P. O'Brien, A. Morbidelli, H. F. Levison, *Icarus* **184**, 39 (2006).
24. R. M. Canup, *Science* **307**, 546 (2005).
25. J. J. Salmon, R. M. Canup, *Lunar Planet. Sci.* **XLIII**, 2540 (2012).

**Acknowledgments:** SPH simulation data are contained in tables S2 to S5 of the supplementary materials. Financial support for this project was provided by the NASA Lunar Science Institute and by NASA's LASER program.

### Supplementary Materials

www.sciencemag.org/cgi/content/full/science.1226073/DC1  
Materials and Methods  
Figs. S1 and S2  
Tables S1 to S5  
References (26–36)

14 June 2012; accepted 1 October 2012  
Published online 17 October 2012;  
10.1126/science.1226073

# How Does Plant Cell Wall Nanoscale Architecture Correlate with Enzymatic Digestibility?

Shi-You Ding,<sup>1\*†</sup> Yu-San Liu,<sup>1\*</sup> Yining Zeng,<sup>1</sup> Michael E. Himmel,<sup>1</sup> John O. Baker,<sup>1</sup> Edward A. Bayer<sup>2</sup>

Greater understanding of the mechanisms contributing to chemical and enzymatic solubilization of plant cell walls is critical for enabling cost-effective industrial conversion of cellulosic biomass to biofuels. Here, we report the use of correlative imaging in real time to assess the impact of pretreatment, as well as the resulting nanometer-scale changes in cell wall structure, upon subsequent digestion by two commercially relevant cellulase systems. We demonstrate that the small, noncomplexed fungal cellulases deconstruct cell walls using mechanisms that differ considerably from those of the larger, multienzyme complexes (cellulosomes). Furthermore, high-resolution measurement of the microfibrillar architecture of cell walls suggests that digestion is primarily facilitated by enabling enzyme access to the hydrophobic cellulose face. The data support the conclusion that ideal pretreatments should maximize lignin removal and minimize polysaccharide modification, thereby retaining the essentially native microfibrillar structure.

Modern biorefineries are being developed to produce transportation fuels from plant biomass using sustainable technologies that also benefit the environment by reducing greenhouse gas emissions (1). The major challenges facing this industry are the high cost of pretreatment and the low efficiency of enzymatic hydrolysis of plant cell wall polysaccharides to sugars. Further improvement of these processes is contingent on deeper understanding of biomass structure and chemistry, as well as improved understanding of the molecular mechanisms of biomass deconstruction (2).

Despite renewed interest in biomass degradation, there is little agreement about which plant cell wall features most affect digestibility by microbes and cellulolytic enzymes. The activities of cellulolytic enzymes are usually characterized by assay against purified or highly modified crystalline or amorphous celluloses, as well as soluble substrates (3). Actual plant cell walls, however, are complex nanocomposites containing networks of cellulose fibrils and complex “matrixing” poly-

mers. The overall performance of biomass saccharification may be attributed to the synergistic action of many complementary enzymes—including a variety of cellulases, hemicellulases, and accessory enzymes (4)—which makes it difficult to study one factor at a time. Traditional solution methods have suffered from the classical ensemble average limitation presented by analysis of these mixtures of complex biomass; therefore, the data gathered are sometimes inconclusive and, in part, contradictory. To overcome these problems, we visualized the action of these enzyme systems on untreated and delignified plant cell walls under controlled digestion conditions in real time with the use of a multimodal microscopy suite, including bright-field light microscopy, confocal laser scanning microscopy (CLSM), two-color stimulated Raman scattering (SRS) microscopy, and atomic force microscopy (AFM). The microscopes were custom-constructed to allow correlative imaging of the same biomass sample under near-physiological conditions and at high chemical (5, 6) and spatial (7, 8) resolutions at the tissue, cellular, and molecular levels. We examined two naturally existing enzyme systems of commercial relevance for saccharification of lignocellulosic biomass: (i) the secretome of the anaerobe *Clostridium thermocellum*, which is representative of multienzyme bacterial cellulosomes (9), and (ii) a commercially available blended enzyme mixture (Cellic CTec2, Novozymes, Bagsvaerd,

Denmark) derived from the fungus *Trichoderma reesei* (*Hypocrea jecorina*), which is representative of the fungal or “free” cellulases (10). We used green fluorescent protein (GFP)-tagged carbohydrate-binding modules (CBMs) to identify exposed cellulose surfaces and green dye (Alexa Fluor 488, Invitrogen, Carlsbad, CA)-labeled enzymes to examine overall cell wall accessibility to cellulases. *TrCBM1* derived from *T. reesei* cellobiohydrolase I (CBH I or Cel7A) (11) and *CiCBM3* derived from *C. thermocellum* cellulosomal scaffoldin protein (CipA) (12) specifically recognize the planar face of crystalline cellulose (8, 13, 14) and play a critical role in the hydrolysis of crystalline cellulose (15, 16).

Naturally senescent, dried corn (*Zea mays* L.) stover stem internode sections served as an example of plant cell wall material. The transverse view of the untreated maize stem represents the typical tissue structure of monocotyledons with scattered vascular bundles (VBs) surrounded by parenchyma cells (fig. S1, A and B). In this context, cell walls in mature plants are generally classified as one of three types: (i) The primary walls (PWs) are thin (~100 nm) and expanded, but are neither elongated nor lignified. (ii) Parenchyma-type secondary walls (pSWs) are found in large parenchyma tissue between the VBs, which are elongated or expanded and partially lignified in the secondarily thickened wall (~1 to 2 μm). (iii) Sclerenchyma-type SWs (sSWs) are elongated and fully lignified in the heavily thickened (~5 to 10 μm) SW. The innermost side of a sSW is often covered by “warts,” which mainly contain condensed lignin-like polyphenols (17). Note that the materials used in this study are from dead plants; cell walls in a living plant may be more structurally complex and diversified.

Using two-color SRS microscopy, where the Raman signal at 1600 cm<sup>-1</sup> (aromatic-ring breathing modes) represents primarily lignin and the 2900 cm<sup>-1</sup> (C-H stretch) band represents primarily polysaccharides (18), we found that the lignin and polysaccharide contents in sSWs were higher than those in pSWs (fig. S1, C to E) and that the polysaccharide content was generally higher in SWs than in PWs. These observations are in agreement with general plant anatomy.

The presence of lignins, a group of highly branched phenylpropanoid polymers found in terrestrial plants, is generally considered to be one of the most important limiting factors in

<sup>1</sup>Biosciences Center, National Renewable Energy Laboratory, Golden, CO 80401, USA. <sup>2</sup>Department of Biological Chemistry, The Weizmann Institute of Science, Rehovot 76100, Israel.

\*These authors contributed equally to this work.

†To whom correspondence should be addressed. E-mail: shi.you.ding@nrel.gov

the enzymatic cell wall saccharification process (19). Whether lignins affect enzyme digestibility by physically impeding or nonspecifically absorbing enzymes remains open to debate. To address this question, we used acid chlorite to produce delignified cell walls. This delignification process has been widely used to produce holocellulose (20). At low temperature, acid chlorite oxidizes phenolic compounds (mainly lignins) in cell walls without altering cellulose and with minimum effect on associated hemicelluloses (5, 21).

As anticipated, we confirmed that accessibility of untreated cell walls to CBMs and enzyme binding exhibits a strong negative correlation with their lignin content. All CBMs and enzymes bind strongly to nonlignified PWs and more weakly to pSWs. Binding to the condensed lignin “warty layer” in sSWs is negligible, indicating that nonspecific adsorption of processed lignin to enzyme reported previously (22) was not observed in the case of a native lignin examined in situ. Lignin removal enhanced overall binding of all probes to lignified walls (i.e., pSWs

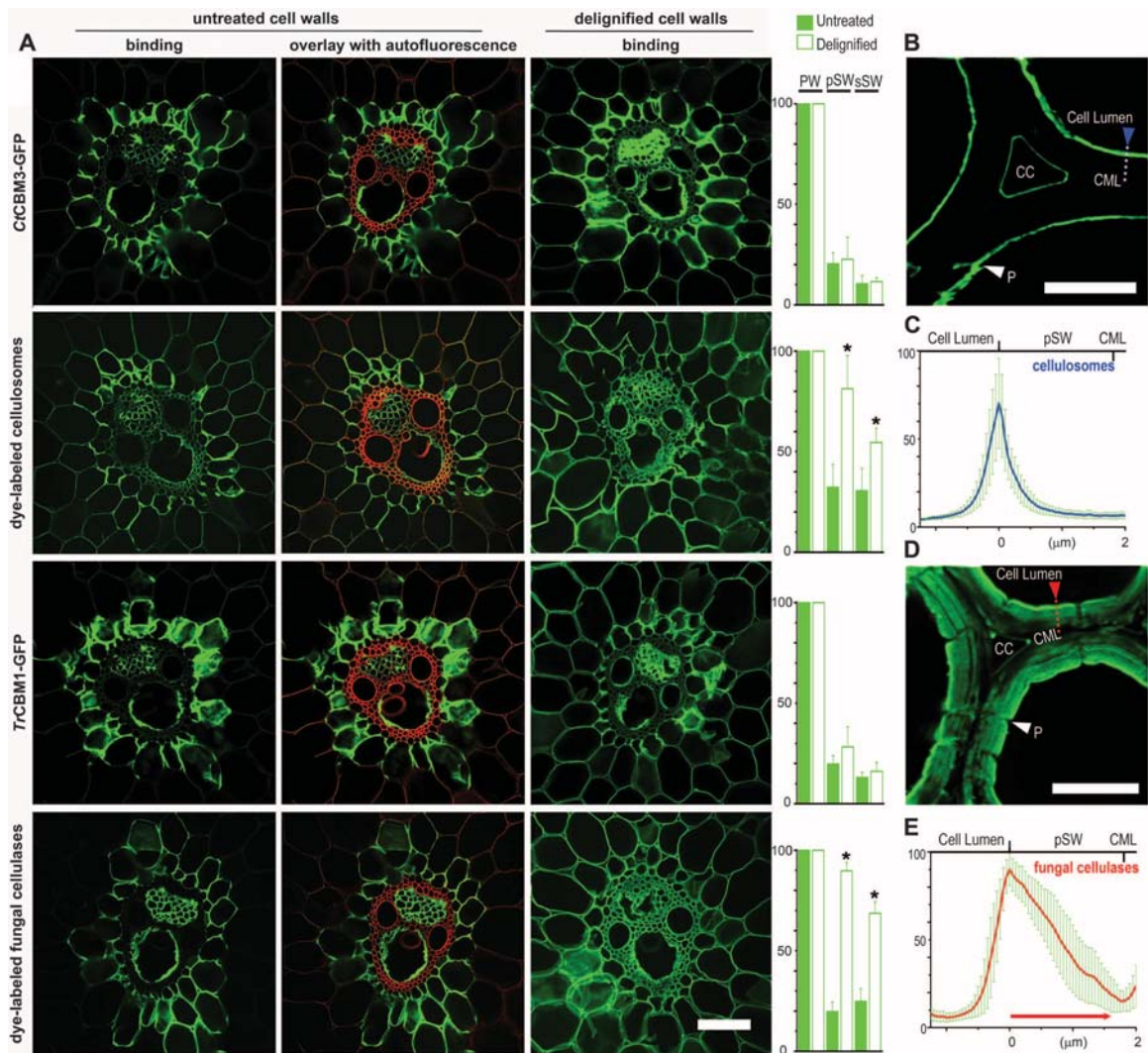
and sSWs) (Fig. 1), following the trend: fungal cellulases (greatest enhancement), cellulosomes, *T*/CBM1, and then *C*/CBM3 (least enhancement). Accessibility of pSWs and sSWs to enzymes was more strongly enhanced than that to CBMs, which could generally be attributed to increased accessibility of hemicelluloses to enzymes after removal of blocking lignins. Further imaging of delignified pSWs by CLSM showed that cellulosomes primarily attached to the surface of the cell walls, the cell corners, and the plasmodesmata (Fig. 1, B and C, and fig. S2A). Fungal cellulases not only bound at these surfaces, but also penetrated inside the SW from its innermost side (Fig. 1, D and E, and fig. S2B), suggesting that delignification may render the cell wall more accessible to fungal cellulases.

After delignification, we found that the lignin signal at  $1600\text{ cm}^{-1}$  was eliminated and the  $2900\text{-cm}^{-1}$  signal was slightly reduced, suggesting that hemicelluloses are generally resistant to acid chlorite treatment at room temperature (Fig. 2, A to E).

The fungal cellulases and cellulosomes that we used in this study contain mixtures of enzymes specific for degradation of different polysaccharide components of cell walls. The digestion temperatures used here were optimal for the fungal ( $38^\circ\text{C}$ ) and cellulosomal ( $55^\circ\text{C}$ ) enzymes. In untreated cell walls, both enzyme systems readily digested PWs only (Fig. 2, F, G, J, and K), and SRS microscopy also revealed minor digestion of pSWs (Fig. 2E and fig. S3). Overall digestibility was strongly negatively correlated with lignin content. Complete degradation was not observed in naturally lignified walls (i.e., pSWs and sSWs), even with 100-fold greater concentrations of enzyme and extended periods of time (7 days).

After delignification, all cell walls were completely digested with the original level of cellulase protein loading (Fig. 2, H and L). Despite the difficulties of quantitatively determining enzyme digestion rates by microscopy alone, we discovered that fungal cellulases acted approximately five times faster than cellulosomes against either untreated or delignified cell walls, based on

**Fig. 1.** Confocal laser scanning microscopy of cell walls exposed to GFP-CBMs and dyed cellulases. All probes are shown in green. (A) Transverse section of VB area. CBMs specifically recognize cellulose, which is highly accessible in PWs but less accessible in pSWs (and is not accessible in sSWs). Autofluorescence (red) and overlay images highlight the negative correlation between probe binding and autofluorescence. Delignification significantly increases cell wall accessibility to enzymes (paired *t* test,  $*P < 0.05$ ). Histograms showing relative fluorescence intensity are expressed as percentages of fluorescence compared with the intensity of the labeled PW, which is designated as 100%. Delignified pSWs in the rind area were imaged in higher magnification. (B) Cellulosomes bound to the pSW innermost surface, the cell corners (CC), and the plasmodesmata (P). (C) Composite-average profile of line scans across the SW, as illustrated by the dotted line in (B). (D) Fungal cellulases penetrating into the pSW from the innermost surface. (E) Composite-average profile of line scans, as illustrated by the dotted line in (D) showing further penetration (red arrowhead). Data are mean  $\pm$  SD based on analysis of five images (A, C, and E). Scale bars: 50  $\mu\text{m}$  (A), 5  $\mu\text{m}$  (B and D).



the percentage loss of SRS signals at  $2900\text{ cm}^{-1}$ . The time needed for complete digestion of the delignified walls apparently depends on wall mass concentration and not on wall types (Fig. 2, I and M). Thinner and less dense walls were digested rapidly, suggesting that the chemical features of the polysaccharides existing in different cell wall types may have less impact on overall digestibility than expected, at least in the case of acid chlorite-treated biomass, in which lignins have been selectively oxidized.

From experiments at room temperature, we made the qualitative observations that the cellulosomes first separated the walls from the compound middle lamella (CML) and then fragmented the walls into segments (Fig. 3A and movie S1), whereas fungal cellulases dissolved the entire wall in a uniform manner (Fig. 3B and movie S2). During the course of digestion by fungal cellulases, the CML remained mostly intact, suggesting that digestion occurred from the innermost side of the cell walls, thus supporting the binding data (Fig. 1D).

We used AFM for real-time imaging of pSW digestion at the microfibril level. In the untreated

cell wall, only a few surface microfibrils were degradable by either of the enzyme systems. After delignification, the cellulosomes appeared to peel off individual microfibrils from the cell wall surface (Fig. 3C and movie S3), whereas the fungal cellulases penetrated inside microfibril networks and made digestion holes or pits (Fig. 3D and movie S4). For quantitative analysis, the surface roughness was expressed by relative Z ranges of AFM images. In the case of cellulosomes, the roughness remained unchanged (Fig. 3E), whereas digestion by fungal cellulases increased the roughness dramatically (Fig. 3F). Individual microfibrils were digested within a few minutes by each of the enzyme systems. Because AFM movies were acquired within a  $1\text{-}\mu\text{m}^2$  scan area, the length of the microfibrils is unknown; therefore, the digestion rate cannot be estimated unambiguously. The wall structure under buffer was similar to that in air with minor differences, consisting primarily of straightening and debundling surface fibrils (fig. S4).

Cellulose represents  $\sim 70\%$  of the total cell wall polysaccharides, and its accessibility to enzymes determines the overall digestibility. We

have previously reported that CBH I binds to and hydrolyzes the hydrophobic planar faces of purified cellulose crystals (8). To further identify the cell wall architectural features that may contribute to differences in accessibility to and digestibility by cellulases, we used nanometer-scale AFM to image untreated and delignified cell walls.

As previously reported, we observed three types of fibrillar structures (7, 23): Ribbon-like macrofibrils, consisting of a number of cellulose elementary fibrils (CEFs), exist in PWs (fig. S5) and on the pSW surface (Fig. 4A and fig. S6). Microfibrils, which contain one CEF and associated hemicelluloses, are predominant in pSWs and sSWs (fig. S7). Although smaller CEFs, such as the 24-chain diamond-shaped model (24), have been proposed, we favor the 36-chain model, primarily based on microfibril size measured directly in the current study and on two primary assumptions: (i) that cell wall cellulose is mostly crystalline and (ii) that the CBM binding face recognizes the cellulose planar face involving three chains (14, 25). Therefore, packing of cellulose I $\beta$  (26) would allow three chains on

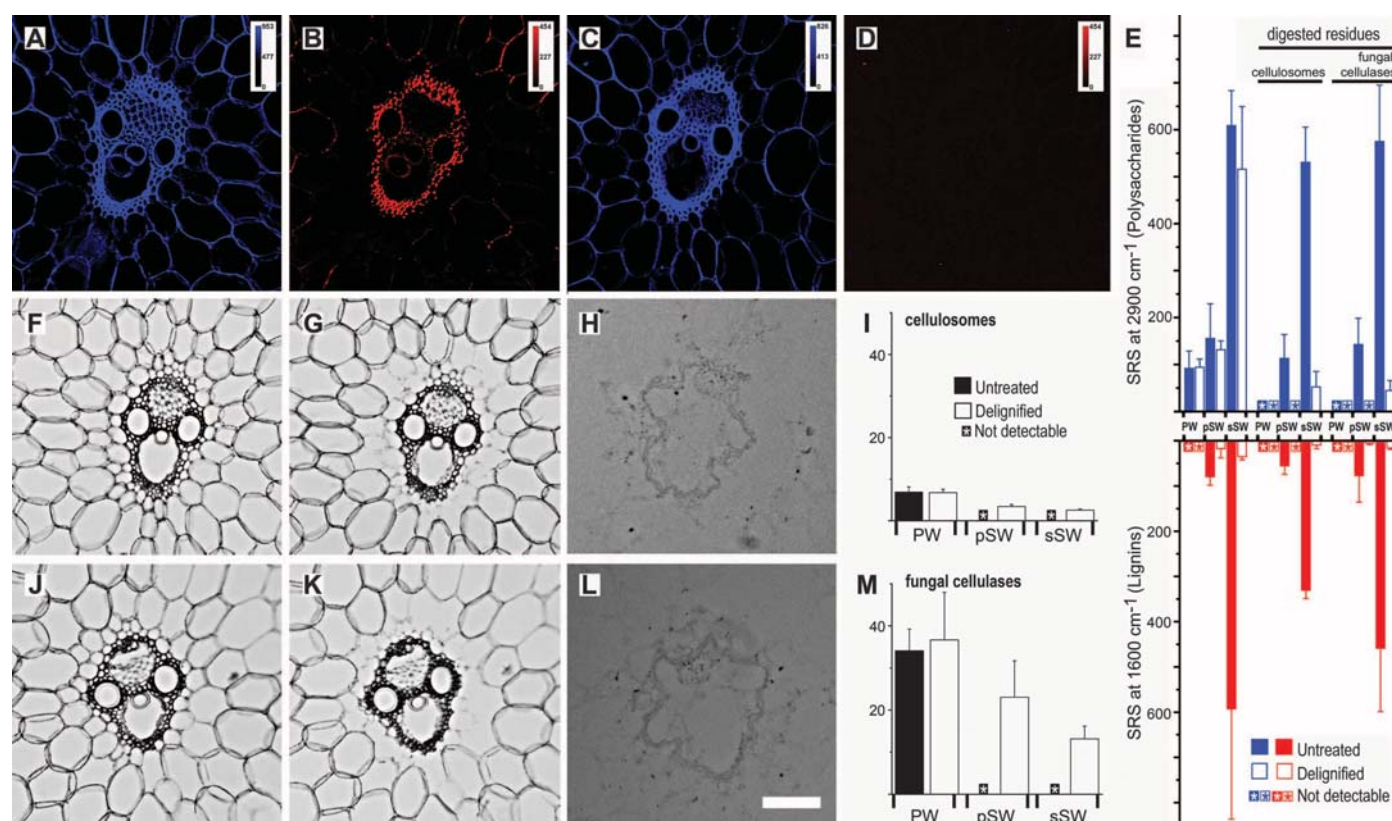


**Fig. 2.** Stimulated Raman scattering (SRS) microscopy of untreated cell walls showing (A) polysaccharides at  $2900\text{ cm}^{-1}$  (blue) and (B) lignins at  $1600\text{ cm}^{-1}$  (red). After delignification, (C) the signal at  $2900\text{ cm}^{-1}$  is slightly reduced, and (D) the  $1600\text{ cm}^{-1}$  signal is eliminated. (E) Histograms of SRS signals in untreated and delignified cell walls and enzyme-digested residues. Bright-field light images of untreated cell walls before (F) and after (G) digestion by cellulosomes for 15 hours at  $55^\circ\text{C}$  showing that only the PWs are completely digested. (H) Delignified walls digested by the cellulosomes for 17 hours at  $55^\circ\text{C}$ , showing that all cell walls are digested. (I) Relative digestion rates by

cellulosomes. (J and K) Untreated cell walls before (J) and after (K) digestion by fungal cellulases for 3 hours at  $38^\circ\text{C}$ , showing that only the PWs are digested. (L) Delignified cell walls are completely digested by fungal cellulases in 8 hours at  $38^\circ\text{C}$ . (M) Relative digestion rates by fungal cellulases. Color bars in (A) to (D) show the lock-in amplifier signals of SRS. Signals that are not detectable are indicated by asterisks in boxes in (E), (I), and (M). Relative digestion rates were calculated based on the percentage loss of SRS signal at  $2900\text{ cm}^{-1}$  per hour (I and M). Data are mean  $\pm$  SD based on triplicate measurements (E, I, and M). Scale bar:  $50\text{ }\mu\text{m}$  (A to L).

the planar faces (100 and  $-100$ ), supporting the 36-chain model.

High-resolution AFM images also allowed precise measurement of the size of fibrillar structures. Isolated microfibrils (Fig. 4A) that appeared twisted were found occasionally on the dry cell wall surface. Note that this twisting effect was not found under aqueous conditions, suggesting that it may be caused by dehydration. In such cases, the AFM line-scan profiles of both vertical (Fig. 4B) and horizontal (Fig. 4C) orientations could be measured on the same CEF. Our measurement of a macrofibril containing two CEFs suggested that they are horizontally associated through their hydrophilic faces (Fig. 4, D and E). Individual microfibrils in pSWs were visualized as sharp edges with bridges partially covering the area between them (Fig. 4, A and D, and fig. S6E), in which the CEF appeared to be primarily vertically oriented. Macrofibril splitting and CEF rotation from horizontal to vertical may occur during cell elongation or expansion (fig. S8).

Quantitative analysis using AFM scan profiles of macrofibrils, microfibrils, and CEFs (Fig. 4F) showed that the widths are slightly larger [ $3.3 \pm 0.5$  nm (vertical) and  $5.7 \pm 0.9$  nm (horizontal)] than those predicted from the 36-chain model (7) [i.e., 3.2 nm (vertical) by 5.3 nm (horizontal)], which may be caused by a combined effect of AFM tip broadening and CEF association with matrix polymers, especially in sSWs (fig. S7C). The microfibrils in the SW appeared to form parallel layers, observed in transverse sections (fig. S7E) and the broken surface in sSWs after delignification (fig. S7I). Cell wall porosity (open space) is measured by three distances between fibrils (5 to 20 nm), layers of microfibrils (10 to 20 nm) (7), and wall lamellae gaps (50 to 100 nm) appearing in the SWs (fig. S7B). Delignification did not substantially alter microfibril structure and arrangement, except for the reduction of matrix polymers of the sSW (fig. S7, G and H).

Schematic structures of the PW and the sandwich-like SW in pSWs and sSWs containing layers of microfibrils and lignin-polysaccharides are illustrated in Fig. 4G. Here, we combine the concepts suggested by the AFM and digestion data, which include the bundling of microfibrils into macrofibrils in PWs and the natural availability of cellulose planar faces in PWs.

These observations of cell wall architecture and microfibril structure are consistent with accessibility to (Fig. 1) and digestibility by (Fig. 2) enzymes, suggesting that the hydrophobic planar face of cellulose is the preferred binding face and thus is critical for enzyme access. In PWs, the CEF hydrophobic faces in macrofibrils are exposed to allow accessibility to cellulases, as confirmed by the strong binding of CBMs and complete digestibility by cellulases. In pSWs, the small surface macrofibrils and microfibrils are accessible, but microfibrils inside the wall are blocked by the lignin-polysaccharide complex

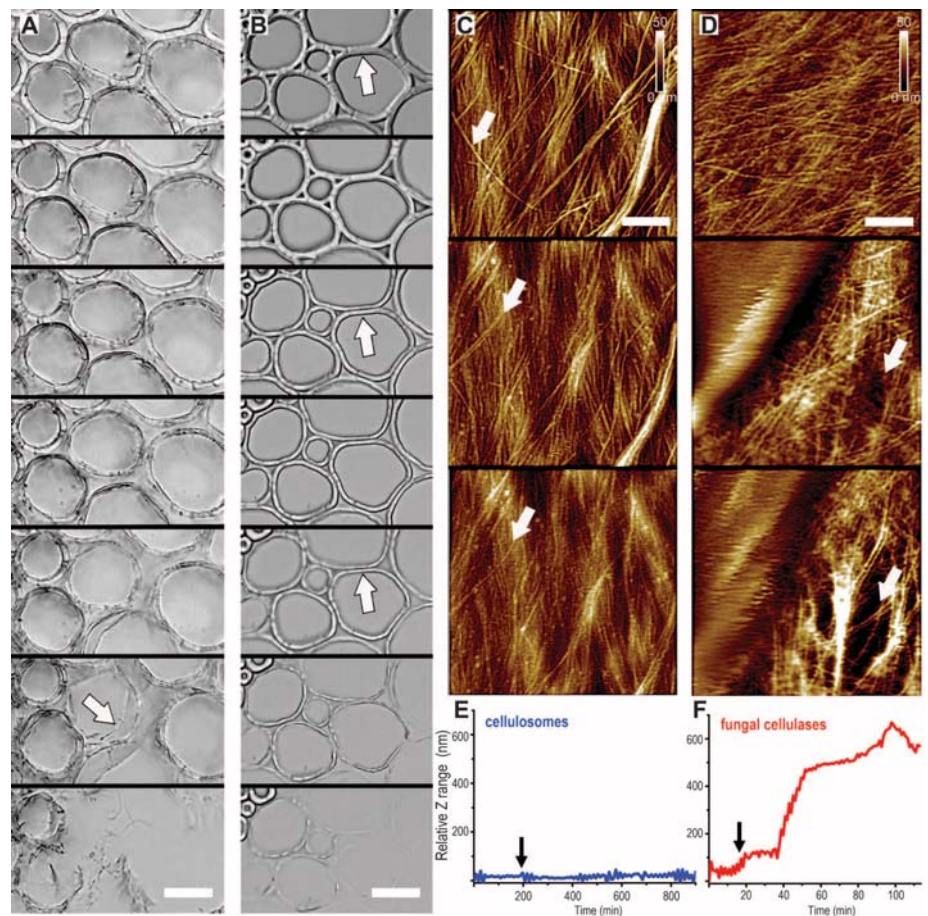


**Fig. 3.** Delignified pSWs imaged in real time during digestion at room temperature. Bright-field light microscopy of a transverse section digested (A) by cellulosomes for 7 days, showing wall fragmentation (white arrow), and (B) by fungal cellulases for 10 hours, showing wall dissolving. White arrows in (B) indicate the wall's innermost side. AFM imaging of a single pSW surface digested (C) by cellulosomes for 13 hours, showing peeling-off of individual microfibrils (white arrows), and (D) by fungal cellulases for 2 hours, showing penetration (white arrows). Images in (A) to (D) were taken from movies S1, S2, S3, and S4, respectively. Relative Z ranges of AFM images were recorded as changes of vertical distance during digestion by (E) cellulosomes (movie S3), showing conserved roughness, and by (F) fungal cellulases (movie S4), showing increasing roughness. Black arrows indicate the time points of enzyme addition. Color bars in (C) and (D) represent the scale of the AFM height images. Scale bars: 50  $\mu$ m (A and B), 200 nm (C and D).

between microfibril layers (Fig. 4G), resulting in diminished CBM binding and limited digestibility by enzymes. In sSWs, lignins form an additional barrier on the innermost side, the condensed lignin warty layer (17), that blocks accessibility of microfibrils to enzymes (Fig. 1), resulting in no digestibility of sSWs (Fig. 2). These observations are also supported by studies on cell wall development, which have indicated that SW thickening begins while the cell is still elongating (27). In later stages of elongation, SW deposition is accompanied by a lignification process that may cause a decrease and eventual cessation of cell elongation. pSWs are not lignified until cessation of vegetative growth in grassy plants; consequently, these walls are completely digestible if harvested during vegetative growth (28).

Acid chlorite treatment effectively removes lignins in the SW (Fig. 2 and fig. S7H) and the

warty layer in sSW (fig. S7F), thereby exposing microfibrils (fig. S7, G to I) to enzyme access, resulting in near-complete digestion of all cell walls. After lignin removal in the SWs, accessibility of the cellulose planar face is then determined by wall porosity. Under the conditions of this study, we observed enhanced digestibility by fungal cellulases due to their penetration into the pore structure of microfibril networks (Fig. 3D and movie S4). In contrast, the larger cellulosome complexes could only penetrate the larger wall lamellae gaps (fig. S7B), resulting in fragmentation of walls (Fig. 3A and movie S1). The advantageous degradation properties exhibited by the fungal cellulases on cell walls may be compromised when digesting purified forms of crystalline cellulose, such as Avicel PH101 (Sigma, St. Louis, MO) (29), in which the porous architecture of the native cellulose microfibril network

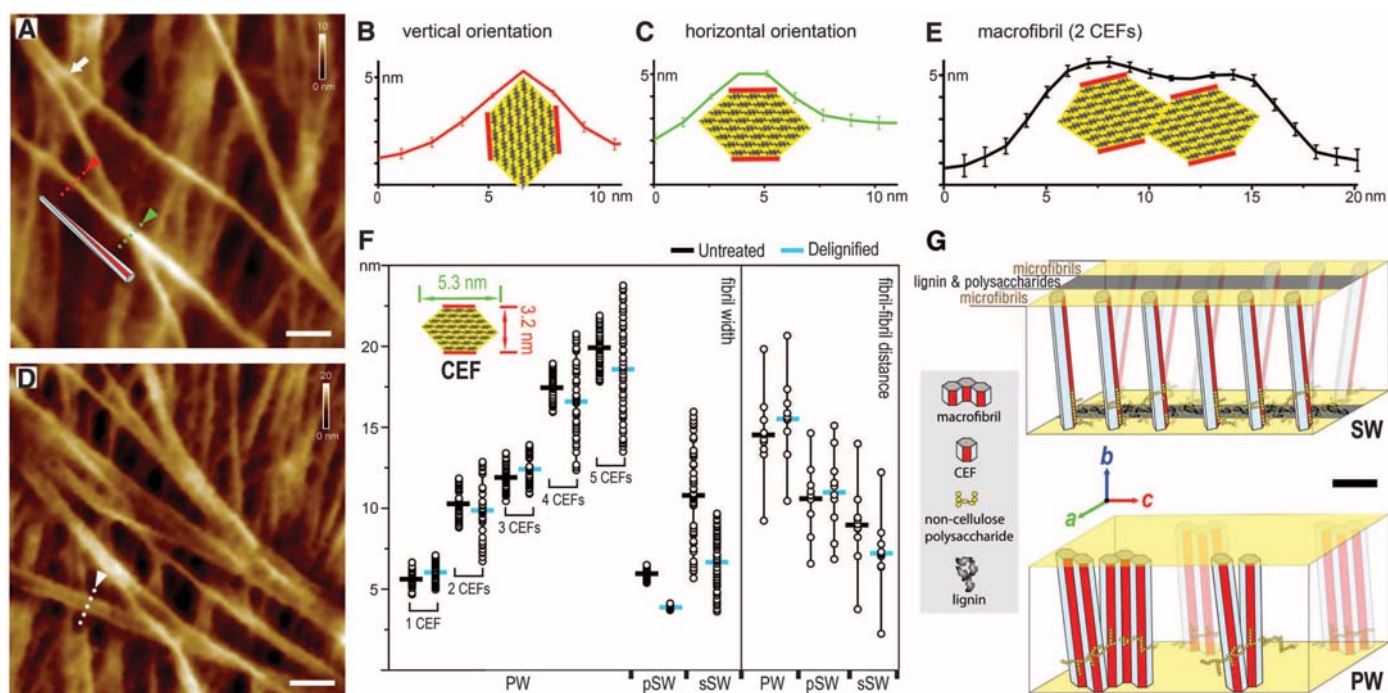


**Fig. 4.** Size, shape, and arrangement of the CEFs. (A) An individual twisted CEF shown in delignified pSW surfaces. Composite-average profile of line scans across the CEF appear in (B) vertical orientation [red dotted-line in (A)] and (C) horizontal orientation [green dotted-line in (A)]. (D) An untreated pSW showing macrofibrils and microfibrils. (E) Composite-average profile of line scans across macrofibrils [white dotted-line in (D)] containing two CEFs. Data are mean  $\pm$  SD based on measurements of five well-defined microfibrils (B and C) and macrofibrils (E). (F) Width measurements of 50 well-resolved fibrils (left) and average fibril-fibril distances measured in the entire image (right). Ten images were measured for untreated and delignified PWs, pSWs, and sSWs. Macrofibril widths containing two to five CEFs in a PW were determined directly by tracing fibril splitting. Horizontal bars denote mean values. (Inset) Dimensions of the 36-chain CEF model are 5.3 nm (horizontal, green arrow) by 3.2 nm

(vertical, red arrow). The hydrophobic CEF faces are indicated in red. Furthermore, one CEF in the PW is expected to display the horizontal orientation, which provides an apparent width of 5.3 nm based on cellulose structure. After delignification in pSWs, the vertical orientation is expected, which provides an apparent width of 3.2 nm. (G) Schematic illustration showing assembly of main cell wall components in the PW and the sandwich-like SW. Scale is based on the average fibril-fibril distance measured in (F). Cell wall orientations are indicated as: (a) transverse and (b) tangential relative to the cell lumen, and (c) cell long axis. Color bars in (A) and (D) represent the scale of the AFM height images; the white arrow in (A) indicates macrofibril splitting. Scale bar: 10 nm (A, D, and G). Additional images showing macrofibrils and microfibrils in untreated and delignified PWs, pSWs, and sSWs are presented in fig. S5 to S7, respectively. The proposed macrofibril splitting and rotating process is shown in fig. S8.

has been completely destroyed during its preparation process. Similarly, it has been reported that biomass digestibility was notably reduced upon near-complete removal of both lignin and hemicelluloses (21). In contrast, the activity of cellulosomes was reported to be higher than, or at least comparable to, that of the fungal cellulases on pure cellulose substrates (30).

Despite the different mechanisms of fungal cellulases and cellulosomes revealed in this study, cell wall materials are completely digestible by either when lignins are effectively removed. Thermochemical pretreatment strategies to enhance biomass digestibility by partial removal or redistribution of lignin have been developed (31), however, these mechanisms result in sugar degradation and loss at high severities (32). The challenge now is to effectively and economically modify lignins via strategies that maintain the integrity of fermentable sugars. Researchers have recently focused on genetically engineering plants for desirable lignin contents or compositions that are more amenable to classical pretreatment at low severities (33–35). In the foreseeable future, we expect that lignins in genetically modified energy plants will be extracted

under mild conditions and used as valuable chemicals; the remaining cell wall architecture could be left intact with minimum alteration of the polysaccharides. In this scenario, effective digestion by enzymes, especially fungal cellulases, could provide near-theoretical yields of fermentable sugars.

#### References and Notes

1. A. J. Ragauskas *et al.*, *Science* **311**, 484 (2006).
2. M. E. Himmel *et al.*, *Science* **315**, 804 (2007).
3. L. R. Lynd, P. J. Weimer, W. H. van Zyl, I. S. Pretorius, *Microbiol. Mol. Biol. Rev.* **66**, 506 (2002).
4. B. Henrissat, H. Driguez, C. Viet, M. Schülein, *Nat. Biotechnol.* **3**, 722 (1985).
5. B. G. Saar *et al.*, *Angew. Chem. Int. Ed.* **49**, 5476 (2010).
6. Y. N. Zeng *et al.*, *Bioenerg. Res.* **3**, 272 (2010).
7. S. Y. Ding, M. E. Himmel, *J. Agric. Food Chem.* **54**, 597 (2006).
8. Y. S. Liu *et al.*, *J. Biol. Chem.* **286**, 11195 (2011).
9. E. Morag, E. A. Bayer, R. Lamed, *Enzyme Microb. Technol.* **14**, 289 (1992).
10. L. E. Berghem, L. G. Pettersson, *Eur. J. Biochem.* **37**, 21 (1973).
11. D. J. Dagel *et al.*, *J. Phys. Chem. B* **115**, 635 (2011).
12. S. Y. Ding *et al.*, *Biotechniques* **41**, 435 (2006).
13. J. Lehtö *et al.*, *Proc. Natl. Acad. Sci. U.S.A.* **100**, 484 (2003).
14. J. Tormo *et al.*, *EMBO J.* **15**, 5739 (1996).
15. N. R. Gilkes, R. A. J. Warren, R. C. Miller Jr., D. G. Kilburn, *J. Biol. Chem.* **263**, 10401 (1988).
16. P. Tomme *et al.*, *Eur. J. Biochem.* **170**, 575 (1988).
17. S. Jansen, E. Smets, P. Baas, *IAWA J.* **19**, 347 (1998).
18. R. H. Atalla, U. P. Agarwal, *J. Raman Spectrosc.* **17**, 229 (1986).
19. R. Vanholme, B. Demedts, K. Morreel, J. Ralph, W. Boerjan, *Plant Physiol.* **153**, 895 (2010).
20. L. E. Wise, M. Murphy, A. A. D'Addieco, *Paper Trade J.* **122**, 35 (1946).
21. C. I. Ishizawa *et al.*, *Cellulose* **16**, 677 (2009).
22. H. Ooshima, D. S. Burns, A. O. Converse, *Biotechnol. Bioeng.* **36**, 446 (1990).
23. D. Harris, V. Bulone, S. Y. Ding, S. DeBolt, *Plant Physiol.* **153**, 420 (2010).
24. A. N. Fernandes *et al.*, *Proc. Natl. Acad. Sci. U.S.A.* **108**, E1195 (2011).
25. J. Kraulis *et al.*, *Biochemistry* **28**, 7241 (1989).
26. Y. Nishiyama, P. Langan, H. Chanzy, *J. Am. Chem. Soc.* **124**, 9074 (2002).
27. C. S. Gritsch, R. J. Murphy, *Ann. Bot. (London)* **95**, 619 (2005).
28. H. G. Jung, M. D. Casler, *Crop Sci.* **46**, 1801 (2006).
29. B. Yang, Z. Dai, S.-Y. Ding, C. E. Wyman, *Biofuels* **2**, 421 (2011).
30. E. A. Johnson, M. Sakajoh, G. Halliwell, A. Madia, A. L. Demain, *Appl. Environ. Microbiol.* **43**, 1125 (1982).
31. B. S. Donohoe *et al.*, *Biotechnol. Bioeng.* **103**, 480 (2009).

32. R. Kumar, C. E. Wyman, *Biotechnol. Bioeng.* **102**, 1544 (2009).  
 33. C. X. Fu et al., *Proc. Natl. Acad. Sci. U.S.A.* **108**, 3803 (2011).  
 34. F. Chen, R. A. Dixon, *Nat. Biotechnol.* **25**, 759 (2007).  
 35. F. Chen, Y. Tobimatsu, D. Havkin-Frenkel, R. A. Dixon, J. Ralph, *Proc. Natl. Acad. Sci. U.S.A.* **109**, 1772 (2012).

**Acknowledgments:** We thank M. P. Tucker for the fungal cellulases; S. Xie for guidance regarding SRS microscopy; K. Ruckman for manuscript editing; and A. J. Ragauskas,

C. E. Wyman, M. F. Davis, D. J. Johnson, and R. H. Atalla for valuable discussion. This work was supported by the U.S. Department of Energy (DOE) under contract no. DE-AC36-08-GO28308 with the National Renewable Energy Laboratory. We acknowledge research support from the BioEnergy Science Center, a DOE Bioenergy Research Center, and the Genomic Science Program (ER65258), both supported by the Office of Biological and Environmental Research in the DOE Office of Science. S.-Y.D. conceptualized the project, conducted AFM, analyzed the data, and wrote the manuscript. Y.-S.L. conducted enzyme labeling, bright-field light microscopy, and CLSM. Y.Z. conducted SRS microscopy. E.A.B. purified the

cellulosomes. S.-Y.D., M.E.H., J.O.B., and E.A.B. revised the manuscript. We declare no competing financial interests.

#### Supplementary Materials

[www.sciencemag.org/cgi/content/full/338/6110/1055/DC1](http://www.sciencemag.org/cgi/content/full/338/6110/1055/DC1)  
 Materials and Methods  
 Figs. S1 to S8  
 References (36–40)  
 Movies S1 to S4

16 July 2012; accepted 21 September 2012  
 10.1126/science.1227491

# Quantum-State Resolved Bimolecular Collisions of Velocity-Controlled OH with NO Radicals

Moritz Kirste,<sup>1\*</sup> Xingan Wang,<sup>1\*</sup> H. Christian Schewe,<sup>1</sup> Gerard Meijer,<sup>1</sup> Kopin Liu,<sup>2</sup> Ad van der Avoird,<sup>3</sup> Liesbeth M. C. Janssen,<sup>3</sup> Koos B. Gubbels,<sup>3</sup> Gerrit C. Groenenboom,<sup>3,†</sup> Sebastiaan Y. T. van de Meerakker<sup>3,1,†</sup>

Whereas atom-molecule collisions have been studied with complete quantum-state resolution, interactions between two state-selected molecules have proven much harder to probe. Here, we report the measurement of state-resolved inelastic scattering cross sections for collisions between two open-shell molecules that are both prepared in a single quantum state. Stark-decelerated hydroxyl (OH) radicals were scattered with hexapole-focused nitric oxide (NO) radicals in a crossed-beam configuration. Rotationally and spin-orbit inelastic scattering cross sections were measured on an absolute scale for collision energies between 70 and 300 cm<sup>-1</sup>. These cross sections show fair agreement with quantum coupled-channels calculations using a set of coupled model potential energy surfaces based on ab initio calculations for the long-range nonadiabatic interactions and a simplistic short-range interaction. This comparison reveals the crucial role of electrostatic forces in complex molecular collision processes.

Rotationally inelastic scattering is one of the key processes underlying the exchange of energy between molecules (1, 2). In bulk systems, rotational energy transfer (RET) is responsible for the thermalization of state populations after a chemical reaction. In the dilute interstellar medium, inelastic collisions contribute to the formation of nonthermal population distributions that result in, for instance, interstellar masers (3). Accurate state-to-state inelastic scattering cross sections are essential ingredients for reliable models of chemical processes in combustion physics, atmospheric science, and astrochemistry.

In molecular beam collision experiments, the ability to prepare molecules in a single rotational (sub)level before the collision using electric, magnetic, or optical fields has been imperative to unravel the underlying mechanisms of molecular energy transfer. This has made scattering exper-

iments possible at the full state-to-state level and has resulted in the discovery of propensity rules for inelastic scattering (4), the stereodynamics of molecular collisions (5, 6), and quantum interference effects (7–9). The latest beam deceleration and acceleration methods (10, 11) allow for the precise variation of the collision energy, resulting in the observation of quantum threshold effects in the state-to-state cross sections (12, 13). This wealth of studies has contributed enormously to our present understanding of how intermolecular potentials govern molecular collision dynamics.

Thus far, these methods have mostly been used to study collisions of state-selected molecules with rare gas atoms. Yet, in most natural environments, molecule-molecule interactions play a major role. For instance, space telescope observations of cometary water may reveal the possible origin of water on Earth, but a conclusive interpretation requires accurate knowledge of RET in water-water collisions (14). Whereas atom-molecule scattering cross sections can now be calculated routinely in excellent agreement with experiment (13, 15), much less is known about RET in molecule-molecule collisions (16). As opposed to an atomic target, a molecular scattering partner possesses internal degrees of freedom of its own, adding a level of complexity that

can easily render ab initio quantum scattering calculations extremely challenging, if not impossible. This is particularly true for collisions involving radical species that are governed by multiple Born-Oppenheimer (BO) potential energy surfaces (PESs) with nonadiabatic couplings between them. Experimental data on bimolecular state-to-state cross sections is generally lacking, and kinetic models often use collision rate coefficients that are expected to be inaccurate (17).

The study of molecule-molecule collisions at the ultimate quantum level has been a quest in molecular beam physics since it was established in the 1950s (18). Major obstacles exist that have prevented studies of state-to-state bimolecular scattering (19). The main challenge is the need for reagent beams with sufficient quantum-state purity at the densities necessary to observe population transfer in one, or both, reagent beam(s). Thus far, experiments of this kind have only been possible using cryogenically cooled H<sub>2</sub> molecules as a target beam (20, 21).

Here, we report the successful measurement of state-resolved inelastic scattering between two state-selected molecular beams. We have chosen the OH (*X*<sup>2</sup>Π) + NO (*X*<sup>2</sup>Π) system (22) for this purpose, as both open-shell radical species are benchmark systems for the scattering of state-selected molecules with rare gas atoms that involve two BO PESs (23). Collisions between OH and NO involve eight interacting PESs, representing the full complexity of bimolecular inelastic collisions (24). The OH-NO system serves also as a prototypical example of radical-radical reactions of fundamental importance in gas-phase chemical kinetics (25). We used a Stark decelerator and a hexapole state selector in a crossed molecular beam configuration to produce reagent beams of OH and NO radicals with an almost perfect quantum-state purity. The collision energy was varied between 70 and 300 cm<sup>-1</sup> by tuning the velocity of the OH radicals before the collision using the Stark decelerator, revealing the quantum threshold behavior of the state-to-state inelastic scattering cross sections. The unusually well-defined distributions of reagent molecules allowed us to determine absolute scattering cross sections, which can normally be determined only on a relative scale in crossed-beam experiments. These cross sections showed fair agreement with a theoretical model for inelastic collisions between two <sup>2</sup>Π radical species, based solely on an accurate description of the full rotational and open-shell structure of both

<sup>1</sup>Fritz-Haber-Institut der Max-Planck-Gesellschaft, Faradayweg 4-6, 14195 Berlin, Germany. <sup>2</sup>Institute of Atomic and Molecular Sciences (IAMS), Academia Sinica, Taipei, Taiwan 10617. <sup>3</sup>Radboud University Nijmegen, Institute for Molecules and Materials, Heijendaalseweg 135, 6525 AJ Nijmegen, The Netherlands.

\*These authors contributed equally to this work.

†To whom correspondence should be addressed. E-mail: basvdm@science.ru.nl (S.-Y.T.v.d.M.), gerritt@theochem.ru.nl (G.C.G.)